Monitoring Ion Therapy with a Compton Camera: Simulation Studies of the Clinical Feasibility

J.-L. Ley[1], D. Dauvergne[3], N. Freud[2], J. Krimmer[1], J. M. Létang[2], V. Maxim[2], M.-H. Richard[1], and É. Testa[1]

[1]Univ Lyon, Université Claude Bernard Lyon 1, CNRS/IN2P3, Institut de Physique Nucléaire de Lyon, 69622 Villeurbanne, France

[2]Univ Lyon, INSA-Lyon, Université Claude Bernard Lyon 1, UJM-Saint Étienne, CNRS, Inserm, Centre Léon Bérard, CREATIS UMR 5220 U1206, F-69373, Lyon, France

[3]LPSC, Université Grenoble-Alpes, CNRS/IN2P3 UMR5821, F-38026 Grenoble, France

E-mail: `jeanluc.ley@gmail.com`

Abstract. The aim of irradiation monitoring during a treatment in ion therapy is to control in real time the agreement between the delivered dose and the planned treatment. In fact, the discrepancies might come from uncertainties such as the planning accuracy by itself, or by variations due to the positioning or the anatomical changes of the patient. This can lead to ion-range variations of a few millimeters. Several devices are under development over the world to detect secondary radiation, which are correlated to the dose deposited by incident ions [1]. Compton cameras are in particular investigated for their potential high efficiency to detect prompt-gammas [2-5]. The present work aims at discussing the clinical applicability of a Compton camera design by means of Monte Carlo simulations validated against measurements of single and coincidence rates.

This first part should be shorter (just speak about treatment uncertainties

There is no validation of the simulation against experimental data. The abstract should provide a summary of the paper results

Submitted to: *Phys. Med. Biol.*

Keywords: Compton Camera, ion therapy, clinical applicability, Prompt gamma

Contents

1. Introduction

The exploitation of the high ballistic precision of hadrontherapy is currently limited by treatment uncertainties such like patient mispositioning, organ motion or morphological changes between treatment fractions. These uncertainties lead to the definition of relatively large safety margins around the planning treatment volume. Moreover the optimal treatment fields with a better sparing of healthy tissues are often discarded to avoid the irradiation of tumor with an organ at risk located downstream. There is therefore a global consensus in the community that ion-range verification is one of the conditions required for a broader usage of hadrontherapy.

Several techniques have been considered worldwide for twenty years. Most of them rely on the detection of secondary radiations generated during nuclear reactions undergone by a fraction of incident ions. Among theses secondary radiations, prompt gamma-rays (PG) has the advantage to be emitted almost instantaneously which could allow for online treatment verification. In addition to this temporal feature, most of PG have well-defined energies corresponding to discrete transitions of incident ions (for ions heavier than protons) or target nuclei (mainly carbon and oxygen). Three observables can be therefore considered: emission point, PG energy and time-of-flight (TOF). Various modalities have been investigated taking benefit from one or several observables: PG imaging with or without collimation (i.e. collimated gamma camera or Compton camera, respectively)

2. Material and methods

2.1. Simulation setup

The monitoring system consists of a beam hodoscope and Compton prototypes under development within a French collaboration (CLaRyS - Contrôle en Ligne avec Rayonnements Secondaires) including five institutions: IPN Lyon, CREATIS Lyon, LPC Clermont-Ferrand, CPP Marseille and LPSC Grenoble. The detectors characteristics can be found in [Krimmer et al., 2015]. For the sake of simplicity, the beam hodoscope is not modeled in this study to focus on PG detection. A scheme of the simulation setup is given in Figure 1.

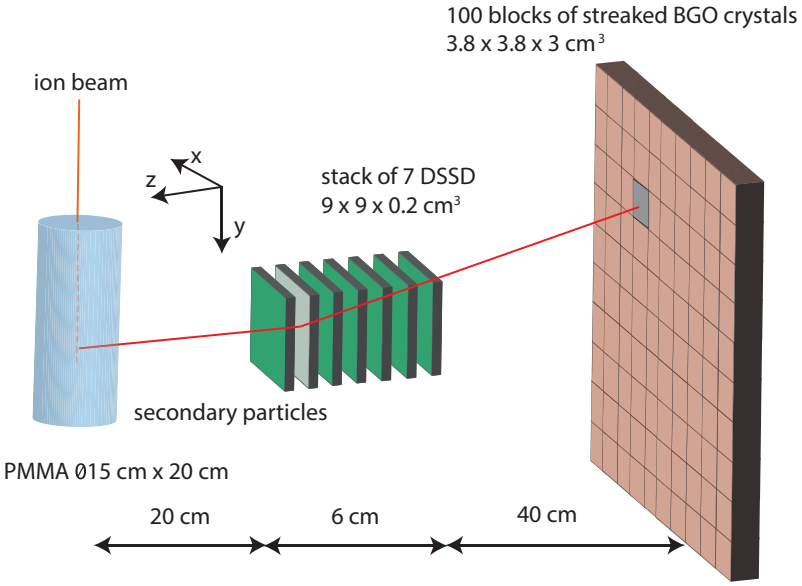

Figure 1: Modelling of the patient (PMMA cylinder) and the Compton camera prototype. The Compton camera is composed of a stack of 7 DSSDs (scatterer) and a plan of 100 single BGO blocks. The distances use are realistic with a clinical treatment. This configuration is used for all the results presented in this paper.

Like most Compton camera devices, the CLaRyS prototype uses a scatterer and an absorber. The scatterer consists of seven parallel planes of silicon detectors (double-sided silicon strip detectors, DSSD) , $9 \times 9 \times 0.2$ cm^3, with 1 cm distance between the centers of two neighboring planes while the absorber is a array of 10×10 BGO blocks ($3.5 \times 3.5 \times 3.0$ cm^3 each block) placed at 40 cm from the last silicon layer. A cylindrical PMMA† phantom is placed in front of the Compton camera to mimic the patient body. This cylinder of 15 cm in diameter and 20 cm in length is set at 20 centimeters in order to fit with a realistic distance to the patient.

Regarding spatial resolution. . .

Detail here how the spatial resolution is modeled (see Mattia's paper.

2.2. Hadronic models used in Geant4

The study is based on the Monte Carlo methods with the Geant4 toolkit, version 9.6 patch 02. Geant4 has been developed by the CERN for the high energy physics experiments. It was shown that it could also be used in ion therapy studies [Cirrone et al., 2011, Toshito et al., 2010]. However, some improvements remains to do in order to adjust the hadronic models [Dedes et al., 2014] . The interaction processes in the matter are described by means of different models according to the type of particles. A resume of those different models is given table 1. Additionally, the Doppler broadening and the polarization is taking into account.

Table 1: Hadronic models used in the Geant4 simulations.

Processus	Protons	Ions	Neutrons
Electromagnetic		$\text{standard}_{\text{option3}}$	
Inelastic	G4BinaryCascade	G4QMDReaction (G4IonsShenCrossSection)	G4BinaryCascade + G4NeutronHPInelastic (<19 MeV)
Elastic	G4LElastic	G4LElastic	G4LElastic + G4NeutronHPElastic (<19 MeV)
Fission	/	/	G4LFission + G4NeutronHPFission(<19 MeV)
Capture	/	/	G4LCapture + G4NeutronHPCapture (<19 MeV)
Radioactivedecay	/	G4Radioactivedecay	/

2.3. Particles of interest

We study the two main particles used in clinics, namely the protons and the carbon ions. The ion range of interest is 15.2 cm in the PMMA target. The energy associated with the range is 160 MeV for the protons and 305 MeV/n for the carbon ions. The beam delivered during a real treatment has a Gaussian profile at the enter of the patient. The standard deviation for a proton beam is 5 mm at 160 MeV and 3.5 mm for a carbon ion beam at 305 MeV/n. The modelling of the Compton camera does not change with the type of incident particles. The statistic for a spot in pencil beam scanning (PBS) mode for protons is 10^8 particles and 10^5 particles for carbon ions. The beam time structure is applied during the post treatment.

2.4. Data treatment

2.4.1. Detector resolutions The Monte Carlo simulation parameters are as close to reality as possible in order to get relevant results. The detector resolutions play an important role in the Compton camera performances. The absorber's spatial resolution influences the position of the apex of the Compton cone and influences its axis orientation. The energy resolution has effect on the Compton cone aperture angle

† PolyMethylMethAcrylate
† Bismuth Germanate

and the timing resolution impacts the coincidence windows between the absorber and the scatterer. The hodoscope is not included in the simulation but its timing resolution is taking into account for the time of flight discrimination. The detector resolutions are modelled in relation to the resolutions measured or estimated for each detector. The spatial resolution, the energy resolution and the timing resolution are presented in the table 2.

Table 2: Estimations of reachable resolutions with the detectors. Those resolutions are applied during the simulations.

Resolution (FWHM) at 1 MeV	**Scatterer**	**Absorber**	**Hodoscope**
spatial [mm]	0.9	5	/
energy [%]	2.3	17	/
timing [ns]	15	3	1

2.4.2. Modelling of the ion beam structure The beam time structure should have a direct impact on the Compton camera capacities to detect a particle in coincidence between the scatterer and the absorber. Two beam time structures have been modelled: one of IBA cyclotron C230 for protons (used in 16 clinical centers worldwide) and one of synchrotron installed at the Heidelberg Ion Therapy Center (HIT) in Germany for carbon ions. Depending on the ion energy and the beam intensity, the beam microstructure will change. We are focusing in this study to the microstructure at a specific energy and also at the influence of the variation of the intensity. In the case of protons at 160 MeV, the ions are grouped in bunches of 2 ns at a frequency of 106 MHz (9.42 ns) [F Roellinghoff, 2014]. The clinical beam intensity is 3.2 nA which corresponds to about 200 protons per bunch. Concerning the carbon ion beam at 305 MeV/u, the estimated microstructure is a bunch of 30 ns at a frequency of 5.9 MHz (170 ns). The clinical beam intensity for carbon ions is 5×10^7 ions/s which corresponds to about 9 ions per bunch. This beam structure is extrapolated from measurements done by our team in 2013 at HIT. The time beam structure was measured for 200 MeV/u and 400 MeV/u carbon ion beams with a two scintillating fiber hodoscope and the spill signal given by the accelerator. The figure 2 shows the beam structure for carbon ions at 400 MeV/u. The pulses have a spill period of 150.2 ns and a bunch is 21.5 ns. A dedicated measure should be done for the energy of interest for this study (305 MeV/u).
Moreover, the measurements have shown that the spill phase change during the extraction which involves the HF signal from the synchrotron can not be used to locate the pulses. The use of the hodoscope seems required.

Concerning the coincidence between the scatterer and the absorber, we allow a time window of 40 ns around an absorber event. It means that for an event detected in the absorber, it will be flagged as a coincidence if an event (corresponding to a deposit

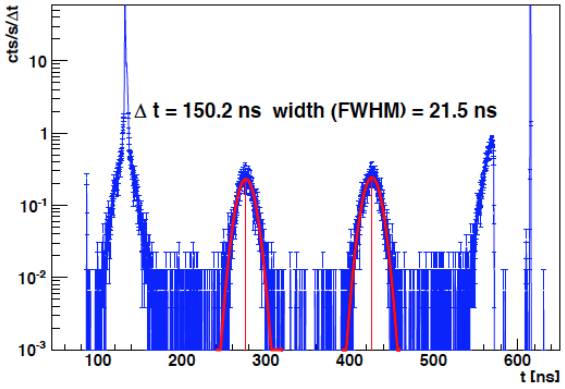

Figure 2: Time structure measured from a carbon ion beam at 400 MeV/u delivered at HIT. The pulses have an extraction period of 150.2 ns and the bunches are 21.5 ns FWHM. The measure was done with a two scintillating fiber hodoscope.

energy) in one the scatterer layers is detected in a window of -20 ns and + 20 ns around the absorber event. This coincidence windows is defined regarding of the silicon timing resolution which is 15 ns at the full width at half maximum. The table 3 resumes those characteristics for specific ions.

Table 3: Description of the two beam structures studied: the IBA cyclotron C230 for protons and the synchrotron installed at the Heidelberg Ion Therapy Center (HIT) in Germany for carbon ions. The beam structures are applied to the simulation data.

		Protons	**Carbon ions**
Clinical characteristics	**Facility**	IBA Cyclotron C230	Synchrotron at HIT
	Clinical intensity	2×10^{10} p/s	5×10^{7} ions/s
	Energy	160 MeV	305 MeV/u
Beam structure	**Bunch time [ns]**	3.2	30
	Period [ns]	9.4	170
	Particles/bunch	217	9
Detectors	**Coincidence window [ns]**	40	40
	Timing resolution [ns]	Si: 15 and BGO: 3	

2.4.3. Coincidence The Compton camera is based on a double interaction inside the scatterer and the absorber. A coincidence is defined as one energy deposit in the scatterer and one energy deposit in the absorber in a coincidence time windows given. A number of coincidence will be considered as background: quasi-simultaneous interaction from two secondary particles or a double interaction from the same particle different from a gamma.
If a coincidence is detected but the two particles are not coming from the same incident ion, the coincidence is named fortuitous. Otherwise, if a single particle from the same incident ion leaves energy in the absorber and the scatterer, the coincidence is named true.
It can be distinguish two types of true coincidence: a single gamma ray, which is a true gamma, and the rest of possibilities (electron, proton, neutron) which is background. The coincidences of interest are the true gamma.

The figure 3 resumes the different definitions of coincidendes in the Compton camera.

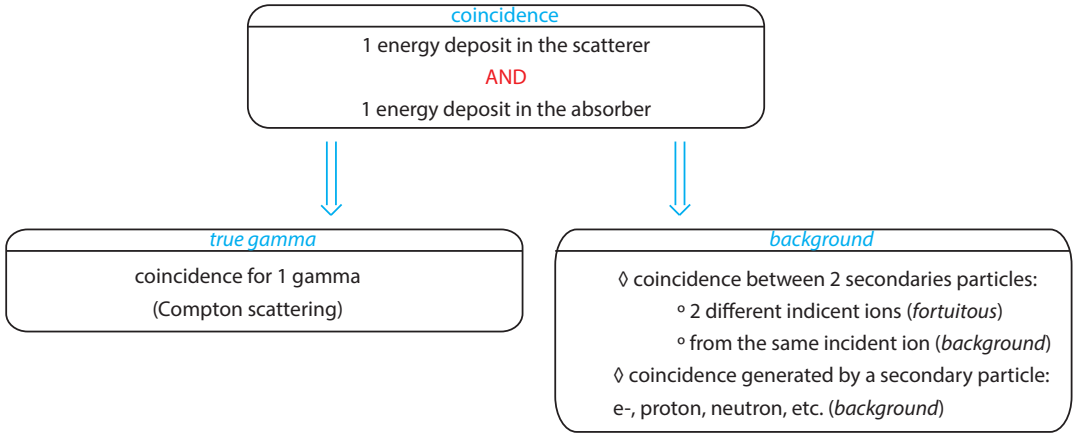

Figure 3: Diagram showing the different definitions of coincidences in the Compton camera.

2.4.4. Time of flight discrimination and energy cuts *Time of flight (TOF) information*

The goal is to eliminate the massive or charged particles (proton, electron, neutron) creating a coincidence in the Compton camera thanks to their speed. In fact, the photons are moving at the light speed when the other particles are moving slower due to their mass. To discriminate the particles with their speed, the time information coming from the hodoscope and the time information coming from the absorber are used. The difference between that information is named time of flight (equation 1). However, the hodoscope is not modelling in this study. As the Monte Carlo code consists to follow all stories individually, the time between the incident particle's creation and the secondary particle detection in the absorber is considered as the time of flight. Moreover, the

hodoscope has a timing resolution about one nanosecond at full width at half maximum, so it is taking into account in the TOF estimation.

$$TOF_{theoretical} = t_{absorber} - t_{hodoscope}$$
$$TOF_{simulation} = t_{absorber} + t_{creation} + u_{hodoscope}$$

With $u_{hodoscope}$ the hodoscope resolution modelled by a Gaussian with a sigma of 1/2.35 ns.

The time of flight spectrum resulting from the simulation shows that the coincidences of interest are included in a window between 0 and 6 ns (figure 4). Therefore, all the coincidences with a TOF higher than 6 ns will be excluded from the results.

Figure 4: Time of flight spectrum obtained by means of the simulation for a proton beam at 160 MeV and 1×10^8 incident protons. The detection time for the absorder is given by the tag for the first deposit energy. The blue curve represents the time of flight for true events and the black one represents the background.

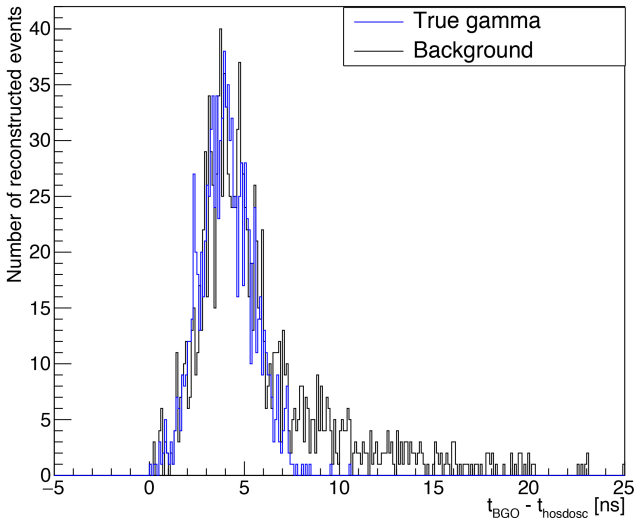

Energy cuts

Energy triggers are also defined for the detectors: 50 keV for the silicon layers and 100 keV for the absorber. An additional energy cut is practiced to the total energy absorbed in the camera and it is set at 1 MeV. In fact, the main gamma rays of interest have an energy upper at 1 MeV.

2.5. Reconstruction algorithm

2.5.1. Line-cone algorithm A simple method is used to reconstruct the emission position of the events detect in coincidence: the reconstruction line-cone. Thanks to the

deposited energies in the detectors and the interaction positions, a cone is calculated which contains the event emission point. The energies enable to calculate the aperture of the Compton cone by way of the following equation:

$$cos(\theta_{Compton}) = 1 - m_e c^2 \left(\frac{1}{E_{absorber}} - \frac{1}{E_{initial}} \right) \quad (1)$$

With $E_{initial} = E_{absorber} + E_{silicon}$
$E_{absorber}$ the energy deposited in the absorber and $E_{silicon}$ the energy deposited in the scatterer.

We assume that the initial energy of the gamma ray is fully absorbed in the absorber. This hypothesis combined to the detector energy resolutions lead to a potential uncertainty on the cone aperture. The interaction position in the scatter gives the cone apex and the position in the absorber gives the cone axis. The intersection of all the reconstructed cones gives the emission source point. In order to simplify the reconstruction and limit the possibilities, the beam direction is used to obtain just two solutions: the beam direction intersects the cone in two points. Only one of those solutions is the good one and the other will give a wrong information. As the original position is unknown when the gamma ray is detected in coincidence, the results presented in the next section take into account the two solutions.

2.5.2. LM-MLEM algorithm The iterative method allows to get a 3D image and allows to take into account the spatial resolution and the energy resolution of the detectors. Few iterative algorithms have been developed for the hadrontherapy [Schone et al., 2010, Zoglauer et al., 2011, Gillam et al., 2011, Mackin et al., 2012, Lojacono et al., 2013].

The iterative algorithm *List-Mode Maximum Likelihood Expectation Maximization* (LM-MLEM) is a MLEM version which allows to free from sinograms and to reconstruct the image directly from the list of events detected.
The objective is to find the emission point of the gamma ray which produces the coincidence detected in the Compton Camera. The first step is to define the volume which includes the origin of the prompt gamma ray detected. This volume is divided in equal voxels and the emission intensity is assumed homogeneous for each voxel j and follows a Poisson distribution of parameter λ_j. The vector contains the emissions intensities of all the voxels and the algorithm has to work it out. The system matrix T is composed of the coefficients t_{ij} which represents the probability that a photon produce by the voxel j is detected as a coincidence i by the Compton camera. The probability for a gamma detected in coincidence to be emitted by the voxel j is s_j. The LM-MLEM algorithm starts with an initial value $\lambda^{(0)}$, which can be the simple backprojection. The algorithm iterations are given by the following recurrence relation:

$$\lambda_j^{(l+1)} = \frac{\lambda_j^{(l)}}{s_j} \sum_{i=1}^{N_\gamma} t_{ij} \frac{1}{P_i^{(l)}}, \quad \text{avec} \quad \mathrm{P_i^{(l)}} = \sum_{\mathrm{k}=1}^{\mathrm{N_v}} \mathrm{t_{ij}} \lambda_{\mathrm{k}}^{(\mathrm{l})}, \quad (2)$$

where N_γ is the number of detected events and N_v is the number of voxels in the image.

The LM-MLEM algorithm uses for this study is the one developed by the labortarory CREATIS in Lyon [Maxim et al., 2009, Lojacono et al., 2013, Maxim, 2014, Hilaire et al., 2014].
For each photon detected, the matrix T is calculated by taking into account the uncertainties on the angle between the source and the scatterer and the angle between the scatterer and the absorber. The matrix elements t_{ij} are calculated by:

$$t_{ij} = K(\beta_i, E_{tot}) \frac{|\cos(\theta_{\overrightarrow{V2V1}})|}{V_2 V_1^2} \int\limits_{M \in v_j} \frac{|\cos(\theta_{\overrightarrow{V_1 M}})|}{V_1 M^2} h_i(M) dv, \tag{3}$$

where β_i is the Compton scattering angle, V_1 the interaction position in the scatterer, V_2 the interaction position in the absorber, h_i the spatial kernel which models the uncertainties on the Compton angle for each voxel M, $K(\beta_i, E_{tot})$ the differential cross section and v the reconstructed volume.

In order to simplify and speed up the work out of the t_{ij} matrix, the voxels located far from the cone are set to 0. The distance between the cone and the voxel is calculated for the center of the voxel. The spatial resolutions are not considered for the algorithm. The images are finally created from the matrix T thanks to Matlab software.

2.6. Precision estimation

It is critical to know the Compton camera precision in clinical conditions in order to associate a decision threshold during the treatment. The precision is equivalent to a shift between the treatment planning (reference) and the reality. The study compare the relative position between a reference profile (reconstructed emission vertex profile at high statistics) and profiles at lower statistics. The analysis is done for a reference profile obtained from an analytic (line cone) and an iterative (LM-MLEM) algorithms. The high statistic profile obtain with the line cone method corresponds to 2×10^{10} incident protons (figure 5a) and the one with the LM-MLEM method correspond to 1×10^{10} incident protons (figure 5b). The *SmoothKern* method, with the Nadaraya-Watson regression, is used to smooth the reference profiles in order to minimize relative statistic fluctuations.
The region of interest (ROI) is from $y = 0$ mm to $y = +100$ mm knowing that the Bragg peak is located around $y = +50$ mm. The reference profiles are modelled in the ROI by a linear combination named Non-Uniform Rational Basis Splines (NURBS).
In theory, a new independent profile should be simulated at low statistics. However, to speed up the analysis, a random draw from Poisson's law is done from the NURBS profile (5c and 5d). The low statistics of interest are from 10^8 to 5×10^9 incident protons. The smallest distance between the NURBS profil and a low statistic profile is estimated thanks to the method χ^2. For the χ^2 estimation, the low statistic profile is defined

around the fall-off from $y = +30$ mm to $y = +70$ mm. The minimization process moves the profile at low statistics on 60 mm from -30 mm to $+30$ mm around the initial position with a step of 0.1 mm. At each move, the χ^2 is calculated as :

$$\chi^2 = \sum_{i=1} (y_{sample,i} - y_{NURBS,i})^2, \tag{4}$$

where y_{sample} is the value of the number of coincidences for the low statistic profile, y_{NURBS} is the value of coincidences for the reference profile NURBS (scaled at the same low statistic) and i the step number.
The global minimum correspond to the smallest distance between the two profiles. The figures 5e and 5f show the distribution of χ^2 calculated for a low statistic profile at 10^8 incident protons.
A total of a thousand profiles at the low statistic are generated (named realizations) and the χ^2 minimization is done for all those. The standard deviation of the distribution resulting of the thousand results give the precision of the camera for a given number of incident protons. The figure 5g and 5h show the distributions at 10^8 incident protons for the line cone and LM-MLEM algorithms.

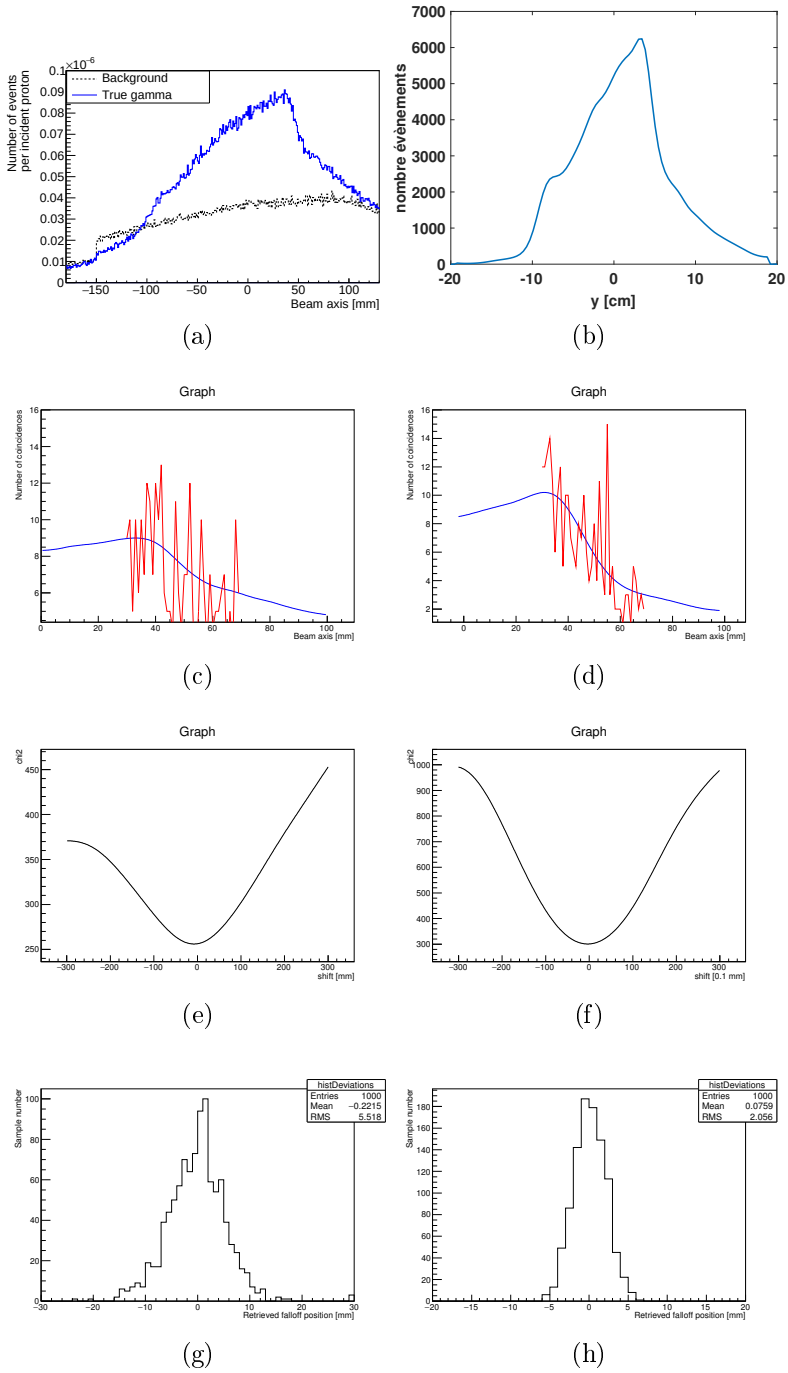

(a) (b)

(c) (d)

(e) (f)

(g) (h)

Figure 5: Treatment comparaison for the same proton simulation with the line cone algorithm (left column: figures 5a, 5c, 5e, 5g) and the LM-MLEM algorithm (right column: figures 5b, 5d, 5f, 5h). The first row give the reconstructed profils for 2×10^{10} incident protons (figure 5a) and for 1×10^{10} incident protons (figure 5b) respectively. The figures 5c and 5d are showing the reference curve (blue) and the estimated curve with Poisson's law at 1×10^{8} incident protons. The figures 5e and 5f are the χ^2 minimization results for one realization. The minimum of the curve gives the best fit between the reference curve and the low statistics one. Finally, the figures 5g and 5h represents the results for 1000 χ^2 minimizations. The Compton camera precision is estimated thanks to the standard deviation of the distribution.

3. Results

3.1. CC efficiency

The absolute efficiency is crucial for the Compton camera performances. It affects directly the number of detected events by the camera and so the reconstruction quality of those events. The absolute efficiency ϵ is defined as :

$$\epsilon = \frac{N\gamma_{recons}}{N\gamma_{total}}, \tag{5}$$

with $N\gamma_{recons}$ the number of gamma events in coincidences,
$N\gamma_{total}$the total number of gamma emitted: 10^8.

The absolute efficiency is presented in function of the localization of a monoenegertic gamma point source in comparison to the Compton camera center. The setup is the same as figure 1, but the point source is in the air and not in a PMMA phantom. The point source is moved from -300 mm to $+300$ mm with a step of 20 mm following the transverse axis of the camera (axis y) and the gamma source is monoenergetic [300 keV, 6 MeV].
The figure **??** shows the absolute Compton camera efficiency in function of the gamma source position. The figure **??** gives the results without any cut in energy on the detectors and the figure **??** is with a cut applied on the energy deposited in the detectors: 50 keV for the scatterer and 100 keV for the absorber.

The absolute efficiency is between 4×10^{-4} at 300 keV and 1.5×10^{-4} at 6 MeV (figure **??**). The efficiency is higher for low gamma energies because the probability of interaction in the absorber is decreasing with the energy. Moreover, when the point source is far from the camera center, the efficiency drops quickly. This effect is marked for high energies. In fact, the incident gamma will be less deflected in the scatterer for the same energy deposited compared to a low energy gamma. The incident gamma of interest in hadrontherapy are around 1 MeV, so it is important to well positioned the Compton camera to optimise the efficiency.
Another aspect to taking into account is the energy cut applied to the detectors (figure **??**). The detectors are not perfect and cuts are mandatory to eliminate the electronic noise. If a gamma has a small Compton scattering angle, the energy deposited in the scatterer will be small. That is why, the camera efficiency decreases when the gamma source is centred with the camera. The limited energy cut is the one applied to the scatterer. This point is important to notice for an application of the Compton camera in nuclear medicine.

3.2. Beam intensity

The beam intensity plays an important role for the Compton camera concerning its capability to distinct events in coincidence. In the simulation, the beam intensity is modeled by an average number of particles per bunch. The exact number of particles

Figure 6: Absolute Compton camera efficiency function of the gamma source position. The figure **??** shows the camera efficiency with no energy cut applied. It models the perfect Compton camera. The figure **??** takes into account cuts in energy: 50 keV for the scatterer and 100 keV for the absorber. The value of the energy cut can be different for the final prototype depending of the detector energy resolutions reach. The analysis is done for energies from 300 keV to 6 MeV.

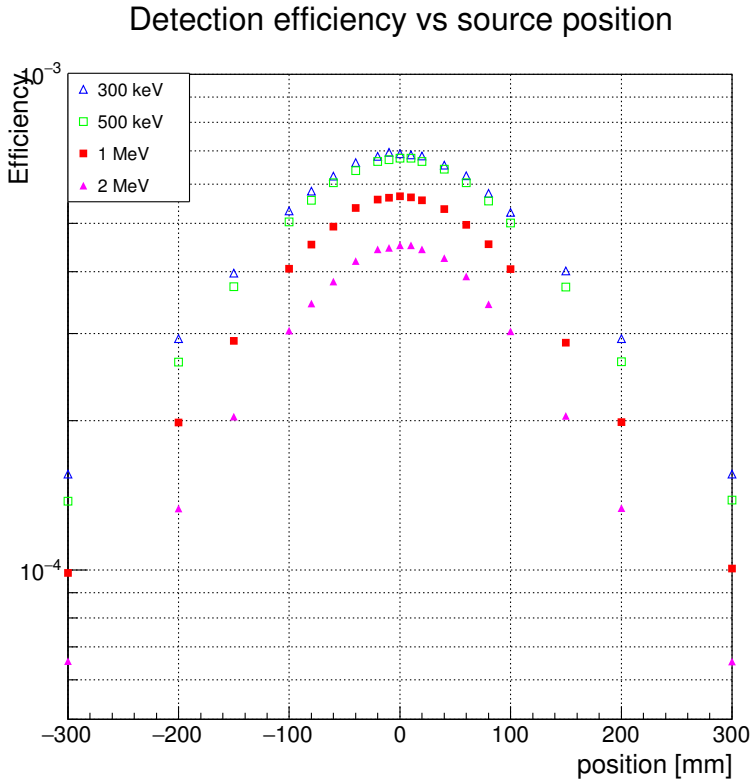

in each bunch is given by a random draw in a Poisson distribution, where the mean value is the beam intensity chosen. The range of intensities was chosen in order to cover almost all the possibilities: from a very low beam intensity to the clinical beam intensity. Therefore, for proton and carbon ion, the lowest beam intensity is set to 0.1 particles per bunch in average and for protons goes up to 217 protons per bunch when in case of carbon ion, it goes up to 70 particles per bunch. The coincidence yields are scaled per ion incidents and the beam intensity per average ions per bunch. The true coincidences represent a coincidence in the camera by the same gamma ray. The background corresponds to all the other coincidence types. The simulations are done for a statistic of 10^8 in case of protons and 2×10^5 for carbon ions. Those statistics correspond to the number of ions used in clinics to treat a spot.

Figure 7: Coincidences yield for protons (figure **??**) and carbon ions (figure **??**) in function of the beam intensity. The intensity is given for a number of incident particles per bunch. The distinction between the filled markers and the empty ones are the time of flight discrimination applied in the case of empty markers. Moreover, the yields are given before and after the profile reconstruction with the line cone algorithm.

(a) (b)

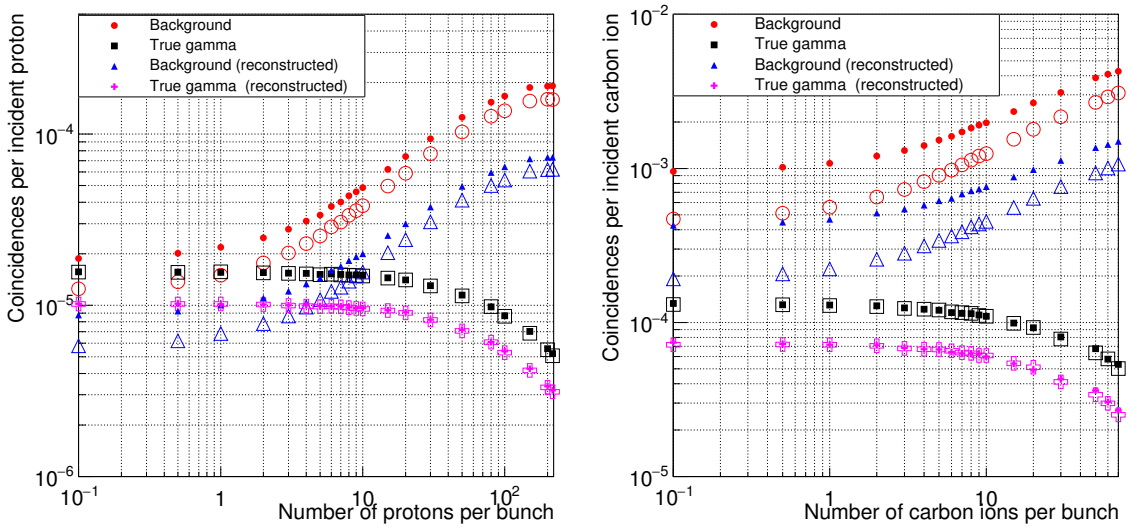

At the clinical beam intensity, the high background level is mainly due to the random coincidences. In fact, the probability to detect two radiation coming from two different incident particles increases with the number of incident particles per bunch. Another issue is the single rate of events detected by each detector at those high intensities. For instance, at the clinic beam intensity in proton therapy, the single rate on the absorber is around 300 MHz and on the first silicon layer it is around 20 MHz. The current electronic front end and acquisition system are not able to treat this amount of data coming from all the detectors. As a result, it appears that it is impossible to use the Compton camera at a clinical beam intensity for the treatment monitoring in ion therapy.

Nevertheless, if the intensity decreases enough to avoid almost all the random coincidences, the monitoring seems more feasible. In addition, it can be supposed that the time of flight discrimination will improve the signal to the background ratio at low intensities by suppressing the coincidences induced by charged particles. Indeed, the charged particles are slower than gamma rays which move at the light speed.

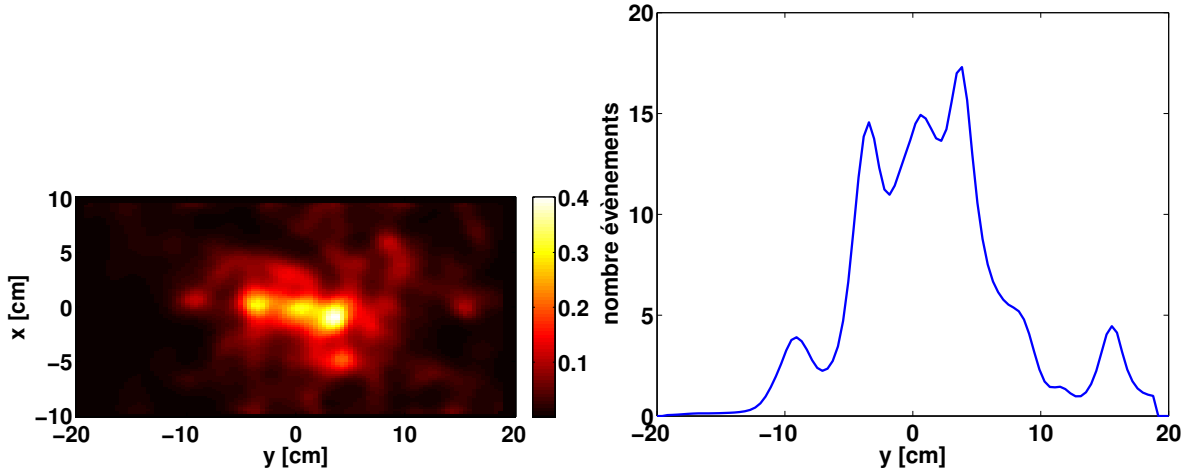

(a) (b)

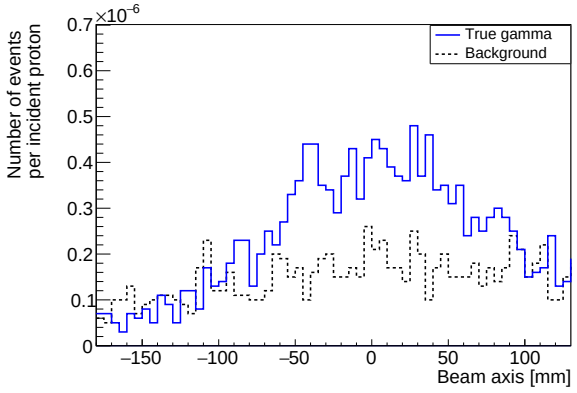

(c)

Figure 8: LM-MLEM reconstruction for a proton beam at 160 MeV and 10^8 incident protons. The events are detected in coincidence and the beam intensity is reduced to 1 proton per bunch. The PMMA target has a diameter of 15 cm and is 20 cm long. The Compton camera is centred at $y = +50mm$. The time of flight discrimination is applied and 20 iterations are realized. The figure **??** represents the reconstruction in 2D for the plan (x,y). The position $x = 0mm$ is the center of the PMMA phantom and y axis the direction of the proton beam. The figure **??** shows the profil corresponding to the figure **??** and following the axis y. The Bragg peak is localized at $y = +50mm$. The figure **??** is the profil obtained by means of line cone algorithm for the same simulation datas.

3.3. Comparaison LM-MLEM vs Line cone reconstruction

3.4. Compton camera precision

The information given by a control device as the Compton camera has to be viable and as precise as possible. In order to estimate the precision of the Compton camera, a method is used.

Figure 9: The Compton camera precision is estimated with two different algorithms: line cone and LM-MLEM. The precision is given for 1×10^8 to 5×10^9 incident protons. A linear fit is realized in order to obtain the slope of the results (p1 parameter). The graphic is scaled in log-log.

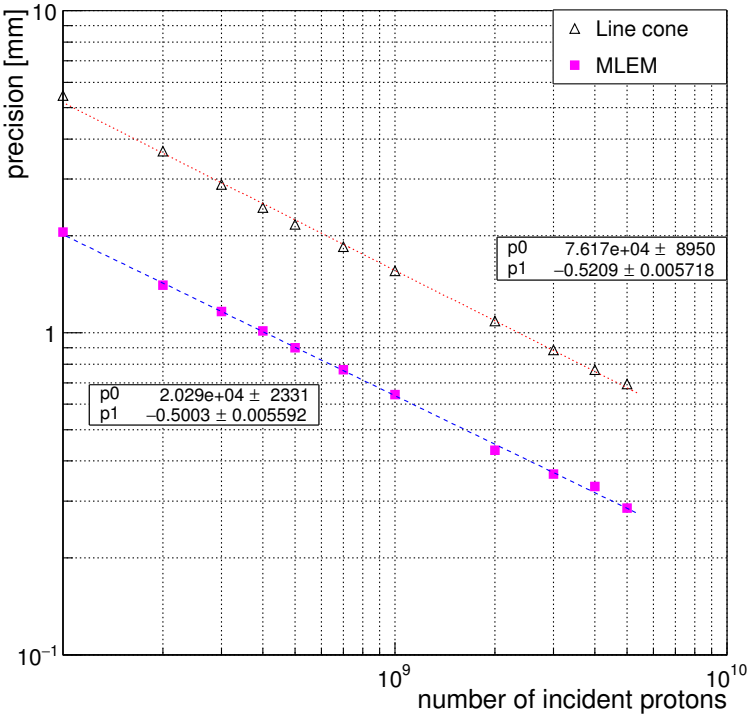

4. Discussion

bla bla

References

[Cirrone et al., 2011] Cirrone, G. P., Cuttone, G., Mazzaglia, S. E., Romano, F., Sardina, D., Agodi, C., Attili, A., Blancato, A. A., De Napoli, M., Di Rosa, F., and others (2011). Hadrontherapy: a Geant4-based tool for proton/ion-therapy studies. *Prog. Nucl. Sci. Technol*, 2:207–212.

[Dedes et al., 2014] Dedes, G., Pinto, M., Dauvergne, D., Freud, N., Krimmer, J., LÃľtang, J. M., Ray, C., and Testa, E. (2014). Assessment and improvements of Geant4 hadronic models in the context of prompt-gamma hadrontherapy monitoring. *Physics in Medicine and Biology*, 59(7):1747–1772.

[F Roellinghoff, 2014] F Roellinghoff, A. B. (2014). Real-time proton beam range monitoring by means of prompt-gamma detection with a collimated camera. *Physics in medicine and biology*, 59(5):1327–38.

[Gillam et al., 2011] Gillam, J. E., Lacasta, C., Torres-Espallardo, I., Candela Juan, C., LlosÃą, G., Solevi, P., Barrio, J., and Rafecas, M. (2011). A Compton imaging algorithm for on-line monitoring in hadron therapy. volume 7961, pages 79611O–79611O–8.

[Hilaire et al., 2014] Hilaire, E., Robert, C., Lojacono, X., Sarrut, D., Buvat, I., Peyrin, F., and Maxim, V. (2014). Compton imaging in proton therapy: reconstructed image of the simulated prompt-ÃÕÂş distribution. In *ICTR-PHE 2014*, page S43, Geneva, Switzerland.

[Krimmer et al., 2015] Krimmer, J., Ley, J. L., Abellan, C., Cachemiche, J. P., Caponetto, L., Chen, X., Dahoumane, M., Dauvergne, D., Freud, N., Joly, B., Lambert, D., Lestand, L., LÃľtang, J. M., Magne, M., Mathez, H., Maxim, V., Montarou, G., Morel, C., Pinto, M., Ray, C., Reithinger, V., Testa, E., and Zoccarato, Y. (2015). Development of a Compton camera for medical applications based on silicon strip and scintillation detectors. *Nuclear Instruments and Methods in Physics Research Section A: Accelerators, Spectrometers, Detectors and Associated Equipment*, 787:98–101.

[Lojacono et al., 2013] Lojacono, X., Richard, M.-H., Ley, J.-L., Testa, E., Ray, C., Freud, N., Letang, J., Dauvergne, D., Maxim, V., and Prost, R. (2013). Low Statistics Reconstruction of the Compton Camera Point Spread Function in 3d Prompt- \gamma Imaging of Ion Beam Therapy. *Nuclear Science, IEEE Transactions on*, 60(5):3355–3363.

[Mackin et al., 2012] Mackin, D., Peterson, S., Beddar, S., and Polf, J. (2012). Evaluation of a stochastic reconstruction algorithm for use in Compton camera imaging and beam range verification from secondary gamma emission during proton therapy. *Physics in Medicine and Biology*, 57(11):3537–3553.

[Maxim, 2014] Maxim, V. (2014). Filtered Backprojection Reconstruction and Redundancy in Compton Camera Imaging. *IEEE Transactions on Image Processing*, 23(1):332–341.

[Maxim et al., 2009] Maxim, V., FrandeÅ§, M., and Prost, R. (2009). Analytical inversion of the Compton transform using the full set of available projections. *Inverse Problems*, 25(9):095001.

[Schone et al., 2010] Schone, S., Shakirin, G., Kormoll, T., Herbach, C., Pausch, G., and Enghardt, W. (2010). A common approach to image reconstruction for different applications of Compton cameras. In *Nuclear Science Symposium Conference Record (NSS/MIC), 2010 IEEE*, pages 2292–2293.

[Toshito et al., 2010] Toshito, T., Bagulya, A., Lechner, A., Ivanchenko, V., Maire, M., Akagi, T., and Yamashita, T. (2010). New Geant4 electromagnetic physics developments for ion therapy applications. In *this conference*.

[Zoglauer et al., 2011] Zoglauer, A., Boggs, S. E., Galloway, M., Amman, M., Luke, P. N., and Marc Kippen, R. (2011). Design, implementation, and optimization of MEGAlib's image reconstruction tool Mimrec. *Nuclear Instruments and Methods in Physics Research Section A: Accelerators, Spectrometers, Detectors and Associated Equipment*, 652(1):568–571.